J Nanostruct 16(3): 3960-3971, Summer 2026

RESEARCH PAPER

Synthesis of Bimetallic Zn–Fe Sulphide Nanoheterostructures with Improved Solar Energy Conversion

Enaas Badr Jawad *, Ahmed K. Abass

Department of Chemistry, College of Science, University of Al-Qadisiyah, Dewanyia 1753, Iraq

ARTICLE INFO

Article History:
Received 19 March 2026
Accepted 26 June 2026
Published 01 July 2026

Keywords:
(Zn–Fe) sulfide nanocomposite
Band gap engineering
Chemical precipitation synthesis
Metal sulfide semiconductors
Photovoltaic performance

ABSTRACT

A novel (Zn-Fe) sulfide nanocomposite semiconductor by facile chemical precipitation method using sodium sulfide as source of sulfide ion. XRD patterns have confirmed the formation of mixed phase composite with the shift in the lattice parameter thus indicating the intimate mixing of Zn and Fe ions in composite structure. Morphology characterization from FESEM and AFM images indicate that the composite is a hybrid structure comprising of ZnS nanoparticles dispersed in the porous framework structure of FeS resulting in larger interfacial contact area and also a larger surface area. Raman spectroscopy has confirmed the occurrence of lattice deformation and interaction of cations within the composite system. Optical study have confirmed the narrowing of band gap value from 2.69 eV of ZnS and 1.30 eV of FeS to 1.77 eV for the composite. Improved absorption in the visible region have been observed for the composite as the band gap is reduced. The electrical transport property of the composite has improved significantly and has an n-type semiconducting behavior with improved carrier mobility and carrier concentration. The TGA-DTG data of the composite shows remarkable improvement in thermal stability with only a weight loss of ~3.36% in the composite system in comparison with the corresponding individual constituents. The power conversion efficiency of composite in photovoltaic cell device measurement found to be 4.2% with greater J sc and FF in comparison to ZnS attributed to the narrowed band gap, reduced recombination, effective charge separation across the junction. The composite is a promising candidate for cost effective photovoltaic device application.

How to cite this article
Jawad E., Abass A. Synthesis of Bimetallic Zn–Fe Sulphide Nanoheterostructures with Improved Solar Energy Conversion. J Nanostruct, 2026; 16(3):3960-3971. DOI: 10.22052/JNS.2026.03.080

INTRODUCTION

The synthesis of metal sulfide semiconductors has received much attention because they possess tunable optical, electrical and catalytic characteristics [1-4]. Thus, they are potential materials for use in photocatalysis, optoelectronics and energy storage applications. Among the metal sulfides, zinc sulfide (ZnS) and iron sulfide (FeS) have been extensively studied because of their low cost, natural abundance and environmental friendliness [2,4].

Zinc sulfide (ZnS) is an II-VI compound semiconductor and has a broad band gap between 3.5 and 3.9 eV [5]. It mainly possesses two common crystal structures which include cubic sphalerite (zinc blende) and hexagonal wurtzite, and these two crystalline structures demonstrate differing optical and electronic properties [3,5]. It

---

* *Corresponding Author Email: enaasbadr700@gmail.com*

has been recognized that control over the phase and morphology (e.g., nanoparticles, nanorods, hierarchical nanostructures) of ZnS plays a role in improving its properties for applications in light-emitting diodes, sensors and photocatalysts [1,3,6,7].

The metal sulfide iron sulfide (FeS) exists in various allotropes including troilite (FeS), pyrite (FeS), marcasite (FeS) and greigite (FeS), and they possess different physical, chemical and magnetic properties due to various crystal structures [8,9]. FeS and their derivatives have potential for battery, supercapacitors, catalysts and remediation applications because of their good electric conductivity and redox characteristics [9,10]. In these structures, different crystalline phase, conductivity and stability have also led to different performance [9]. The synthetic methods have been proved to have great influence over phase and morphology of FeS and hence their applications [8,10].

The composite made up of ZnS and FeS have recently become a growing field and these composites represent a new materialsystem trying to integrate the optical and wide band gap property of ZnS with the electrical conductivity and catalytic activity of iron sulfide [11], [12]. Through formation of heterojunction interfaces of ZnS and FeS, electron-hole recombination can be suppressed efficiently which could lead to improved efficiency for photocatalytic and electrochemical applications [11]. Thus they have the advantages over the individual compound sulfides in performance and stability [12,13].

Several methods of synthesis of ZnS, FeS and their composites including co-precipitation, solvothermal and hydrothermal, and chemical bath deposition have been explored [2,7,14]. Precise control over the phase, particle size and morphology has been achieved by tuning synthetic parameters and these factors significantly influence the properties. Hence the synthesis

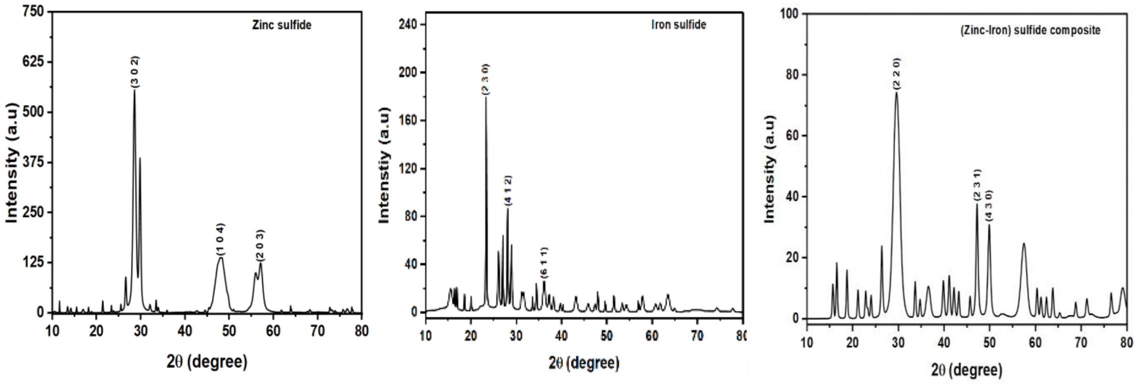

Fig. 1. X-ray Crystal structures of nanomaterials at zinc sulfide, iron sulfide and (zinc-iron) sulfide composite synthesis by sodium sulfide as precipitating agent.

Table 1. X-ray data of zinc sulfide, iron sulfide and (zinc-iron) sulfide composite synthesis by sodium sulfide as precipitating agent.

Nanomaterial		Zinc sulfides	Iron Sulfides	(Zinc-Iron) sulfide composite
Patterson space Group		P1	P1	P2/m
Cell Parameters	α	94.37	100.73	90.000
	β	98.09	94.59	94.293
	Ɣ	100.54	74.12	90.000
	a	8.730	8.889	8.657
	b	6.360	8.122	6.071
	c	5.799	7.179	7.314
Cell volume		311.45	489.50	366.85
Density(g.cm^{-3})		4.36502	4.17511	4.85729

of ZnS, FeS and their composites remains an important area for high-performance functional materials.

MATERIALS AND METHODS

ZnS, FeS and Zn-FeS composites were synthesized by using Na$_2$S as the precipitating agent through a chemical precipitation process. Firstly, the aqueous precursors were prepared by dissolving the needed metal salts in deionized water. For ZnS, 2M ZnCl$_2$ solution was prepared by dissolving 27.26g ZnCl$_2$ in 100mL deionized water. For FeS, 1M FeCl$_2$ solution was prepared by dissolving 16.29g FeCl$_2$ in 100mL deionized water. For the composite sample, mixed solution containing 2M ZnCl$_2$ and 1M FeCl$_2$ was prepared in 100mL deionized water. All the solutions were heated on a hot plate for 30min under constant stirring in order to get uniform solution. In a separate container, 2M Na$_2$S solution was prepared by dissolving 31.22g Na$_2$S in 200mL deionized water and heated for 30min for full dissolution. Dropwise addition of Na$_2$S solution using burette to above solutions (ZnCl$_2$ solution, FeCl$_2$ solution and mixed ZnCl$_2$-FeCl$_2$ solution) was performed until precipitation occurred. PH of the resulting mixture was 2.91, 6.76 and 6.43 for ZnS, FeS and Zn-FeS composite respectively. After precipitaion, the mixture was stirred on a magnetic stirrer at 60 o C for 3 h to ensure that the precipitation is complete. The precipitates obtained were filtered and washed many times with deionized water to remove impurities and the obtained products were dried in oven at 100 o C for 3 h for ZnS, FeS and Zn-FeS composite powder formation.

RESULTS AND DISCUSSION

The XRD diffractograms for the synthesised nanomaterials are shown in Fig. 1. It can be seen that zinc sulfide had 4 diffraction reflections and a peak maximum at 2 = 28.6646 (d = 3.11432). Iron sulfide on the other hand had 7 diffraction reflections, and a peak maximum at 2 = 26.1031 (d = 3.41384). Zinc-iron sulfide had 4 reflections and a peak maximum at 2 = 29.2014 (d = 3.05829). The diffraction shown by these samples is typical for powder diffraction of crystalline solids [15-18].

The identified peaks match with triclinic ZnS, monoclinic FeS and monoclinic zinc-iron sulfide composite phases, following the crystallographic database values [23]. XRD results illustrate the utilization of sodium sulfide (NaS) as sulfide source to obtain the metal sulfides through precipitation-a commonly practiced route of synthesized sulfide nanoparticles [22-24]. Zinc and iron sulfides form crystals in the triclinic structure (space group P1) while the composite material crystallizes in monoclinic (P2/m). This structural transformation is a result of the strong interaction between Zn and Fe ions, causing the crystal lattice to re-organize to an even higher symmetric crystalline phase [22].

Lattice parameters further demonstrate this change. ZnS and FeS shows triclinic shape having no angle 90, while the composite crystal lattice form a monoclinic crystal having two angles 90, consistent to crystallographic laws [22,24]. It shows the lattice distortion because of incorporation of ions in the lattice. The unit cell volume calculated was 311.45, 489.50 and 366.85 for ZnS, FeS and composite, suggesting that the resulting composite material has a mixed lattice rather than physical mixture [17,22] as clearly seen in Tab 1.

The determined densities of ZnS, FeS and composite (4.365 g/cm, 4.175 g/cm and 4.857 g/cm respectively) prove that the atomic arrangement is more packed and stable for the composite

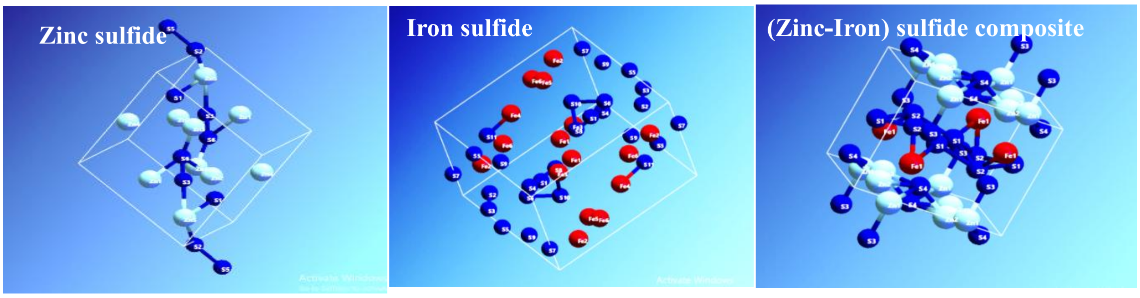

Fig. 2. X-ray Crystal structures of nanomaterials at zinc sulfide, iron sulfide and (zinc-iron) sulfide composite synthesis by sodium sulfide as precipitating agent.

system-a typical property of mixed metal sulfides [22,24]. All these parameters indicate that zinc-iron sulfide nanocomposite have been successfully synthesized having modifications in crystal structure, lattice parameters and improved packing, thus potentially affecting the properties of the composite [15,17].

The crystal structures of nanomaterials are shown in Fig. 2. This figure Shows how the atoms are ordered in the nanomaterial. By seeing how the atoms are ordered it would tell you more about the physical and chemical nature of the material. The order in relation to crystallite size and sintering temperature for nanomaterials is key in the synthesis and characterization of nanomaterials [21,22].

FESEM images were also observed to check the morphological features (shape, distribution and size of particle) of zinc sulfide, iron sulfide and the Zn-Fe sulfide composite. Fig. 3 displays the morphology of zinc sulfide nanomaterials; the particles are nearly spherical with cauli flower-like cluster morphology. The size of the primary particle is from 20-60 nm and some agglomerate can reach to a few hundreds nanometer. Particles are closely distributed and agglomerate tightly because of the

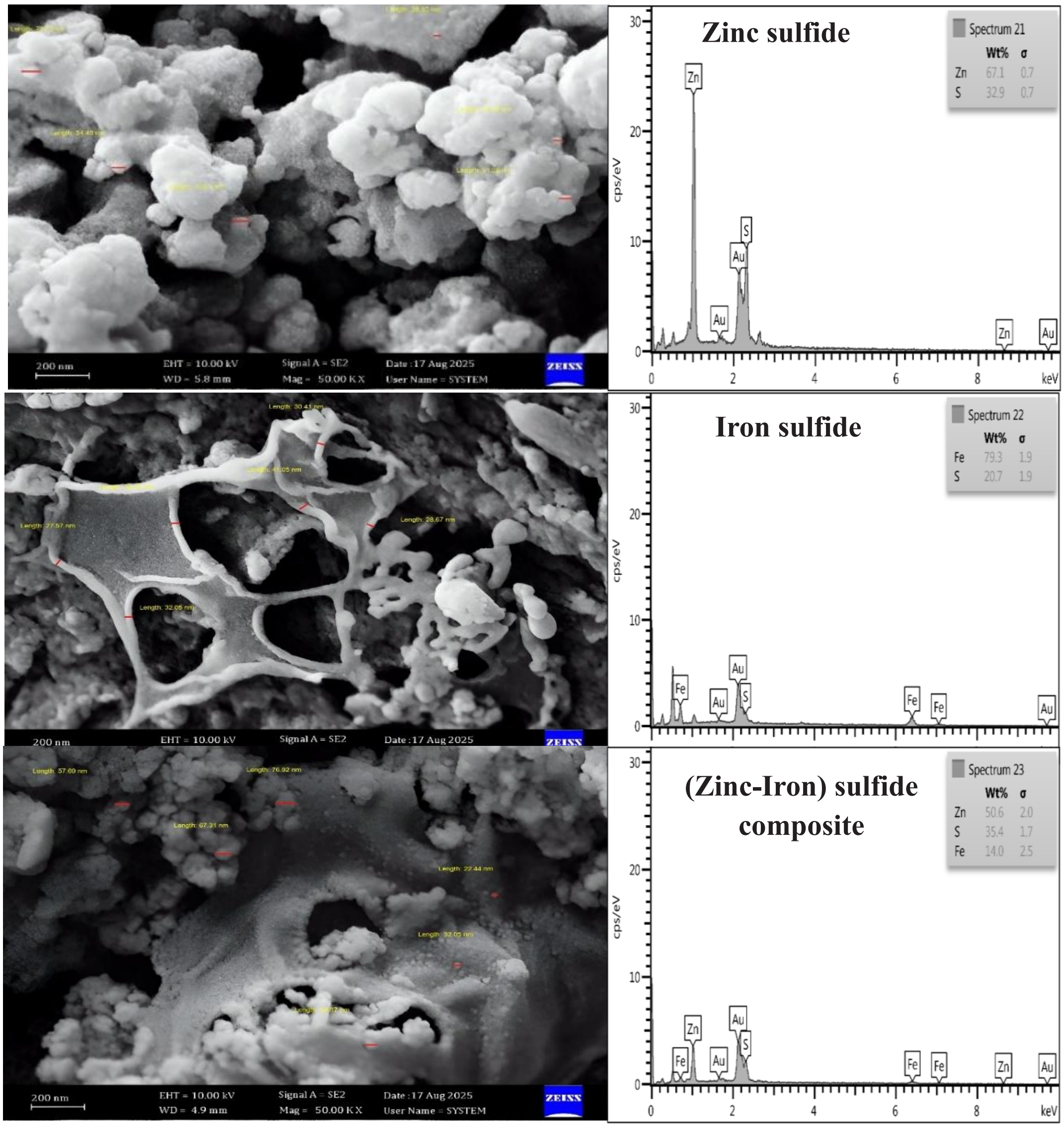

Fig. 3. FESEM micrographs of zinc sulfide, iron sulfide and (zinc-iron) sulfide composite synthesized by precipitation technique.

large surface energy [25,26], morphology is also relatively homogeneous among the field.

But the structure of FeS presents an interconnected pore network instead of separate particles. There are no uniform and regular parts in the porous FeS. The whole is irregular ligament network with cavity structures (30-80 nm in thickness) and distribution heterogeneity is relatively high (Fig. 3) ponge-like structure of is commonly resulted from anisotropic growth under synthesis in solution system [27,28]. As can be seen from Fig. 3, the Zn-Fe sulfide composite takes the shape of hybrid structures: well-dispersed ZnS nanoparticles (25-70 nm) covered on/among a porous FeS matrix structure. The well-dispersed feature suggests strong interfacial contact and mixing ability but moderate heterogeneity still exists since hybrid structure has two different parts. These hybrids greatly promote interfacial area and active sites and hence enhance the function properties [29,30].

EDS also proves the elemental composition of ZnS (Zn, S), FeS (Fe, S) and the composite (Zn, Fe, S). As trace amount of Au peaks in Fig. 3 is result of carbon coating, small fluctuation of stoichiometry should be ascribed to sulfur vacancies or oxidation [31]. Summary, according to FESEM-EDS, ZnS is homogeneous accumulated nanoparticles, FeS is irregular porous network, whereas composite is hybrid structure with favorable interfacial contact.

Zinc sulfide has two typical first order phonon modes at 274 cm^{-1} (TO) and 347 cm^{-1} (LO) attributed to the Zn-S vibrations in cubic zinc blende structure as supported by XRD (PDF 01-077-2100; 00-002-0564). Since this structure possesses high symmetry (F-43m) only TO and LO modes are Raman active, additional broad peaks arise from confinement of phonons and defects (related to nanocrystallinity and sulfur vacancies) [32,33]. Iron sulfide has multiple Raman peaks in the region of 250-450 cm^{-1} attributed to Fe-S vibrations; corresponding to troilite/pyrrhotite structure confirmed by XRD (PDF 00-003-0822; 00-049-1632) [34]. Its low symmetry and the deviation in the stoichiometry (FeS) provide more Raman active modes and the additional peaks between 640-720 cm^{-1} may arise due to multiphonon or defect related phenomena (Fig. 4).

With addition of iron, in the mixed metal sulfides Zn-Fe-S, XRD indicates the presence of an additional mixed metal sulfide phase thus showing a ternary or solid-solution type structure. Raman spectrum of the Zn-Fe-S shows shifts and broadening in the peaks corresponding to Zn-S and Fe-S vibrations and some new peaks. These indicate lattice distortion, replacement of cations (crossover effect) and reduced symmetry causing relaxed selection rules. The defect related and multiphonon scattering is enhanced and facilitated by fast sodium sulfide precipitation, promoting cation mixing in the ternary structure.

Fig. 5 also presents the images from atomic force microscopy (AFM) for surface morphology and roughness of zinc sulfide, iron sulfide and zinc-iron sulfide composite produced using sodium sulfide. A difference in surface morphology, grains distribution and roughness of samples can clearly be seen from the figures. The surface of the zinc sulfide is relatively homogeneous and densified with nanograins spread densely. The roughness is quite small and values for Ra=1.01nm, Rq=1.30nm and Rt=12.38nm is observed in Table 2 that show very smooth nanosurface.

The small Gaussian height distribution is

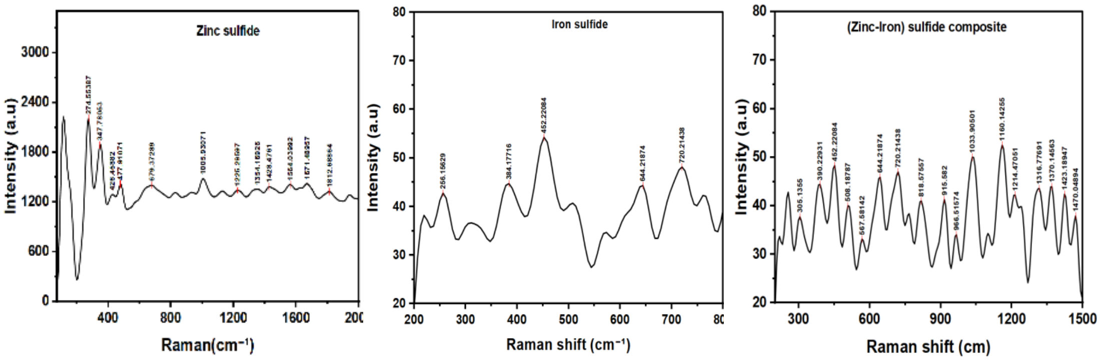

Fig. 4. Raman spectra of zinc sulfide, iron sulfide and (zinc-iron) sulfide composite synthesized by precipitation technique.

indicative of controlled growth and uniform nucleation.Smooth morphologies were previously correlated with stable growth conditions of sulfide nanomaterials [35,36]. In the case of iron sulfide, however, the surface is much rougher and less uniform. The large values of Ra (8.77nm), Rq (10.93nm) and Rt (76.69nm) show considerable variations and undulations of the surface and between features. AFM images indicated large particles agglomerated together with uneven distributions, suggesting rapid nucleation and growth in the alkaline sulfide environment favoring particle growth and agglomeration [37,38].

Intermediate behavior of the zinc-iron sulfide composite as can be observed by the roughness values Ra=7.53 nm, Rq=9.25 nm, Rt=55.89 nm between Zinc and Iron sulfide. And by the morphology a more uniform particle distribution and less aggregation than Iron Sulfide. The growth of iron sulfide seems to be hindered by the incorporation of zinc which promotes a more uniform structure. This behavior has been observed in mixed metal sulfides where cation substitution affects growth kinetics [39, 40]. It suggests that zinc might be acting as a stabilizing factor which is preventing large growth and excessive aggregation. Smooth surfaces of ZnS are good for optoelectronics applications,

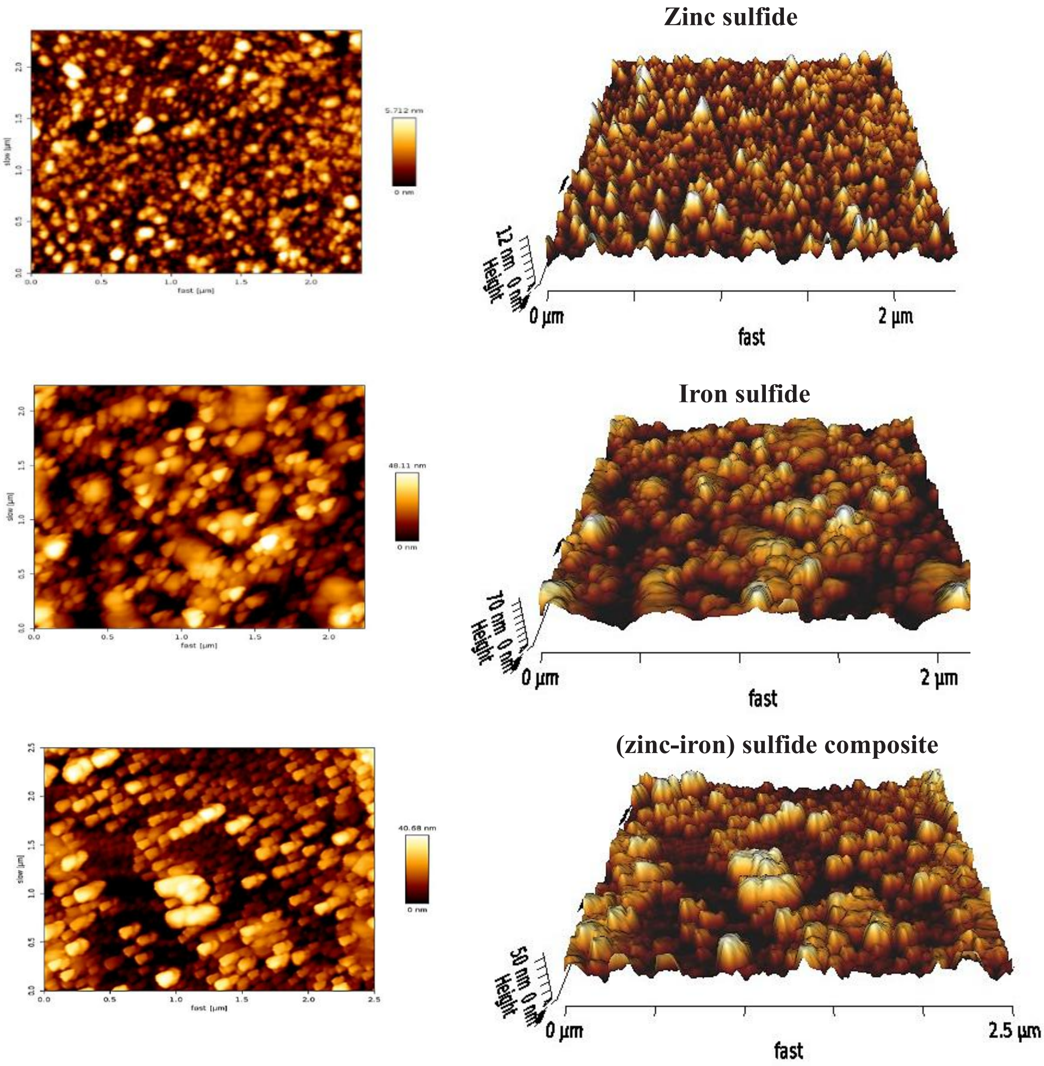

Fig. 5. AFM images of zinc sulfide, iron sulfide and (zinc-iron) sulfide composite synthesized by precipitation technique.

whererough surface of FeS will be beneficial for catalytic properties [36, 38]. A balance between the uniformity and roughness make it suitable for multifunctional applications. This shows AFM confirms that the use of sodium sulfide as the precipitating agent allowed to get surfaces of controlled roughness, and that the incorporation of Zn leads to a significantly improved uniformity and maintainance of nanoscale roughness.

Fig. 6 presents UV-Vis electronic spectra of Zinc sulfide, Iron sulfide and (Zn-Fe) sulfide composite that was synthesized by sodium sulfide. The absorption edges for ZnS, FeS and the composite (Zn-Fe) Sulfide were 461 nm, 954 nm and 700 nm and correspond to band gaps of 2.69, 1.30 and 1.77 eV respectively. The band gaps are calculated using (Eg = 1240/lambda). Zinc sulfide have a rather wide band gap (2.69 eV) with the absorption confined to the UV region. This is smaller compared to bulk Zinc sulfide which is ~ 3.6 eV. The lower band gap value could be related to the formation of defects, sulfur vacancies or the quantum effects at nanostructures which is related to chemical synthesis of the particles [41, 42]. Optical transitions are attributed to transitions between the S 3p valence band and the Zn 4s conduction band, and d-d transitions are forbidden due to the presence of filled Zn 3d orbitals. A sharp absorption edge indicates direct transition and presence of few defect states.

Iron sulfide possesses a very narrow band gap (1.30 eV) with the absorption spanning over the entire range from UV to the visible and even to near-infrared region. This is attributed to electronic states of Fe 3d orbitals and includes charge-transfer transitions (S 3p Fe 3d) d-d transitions and defect states [43, 44]. The existence of a broad absorption tail or Urbach tail implies highly disordered structure with large defect density, therefore suitable for solar energy conversion or photocatalysis applications. The (Zn-Fe) sulfide composite shows intermediate band gap (1.77 eV), and there is a strong interaction between the two sulfides on electronic level. The absorption red shifts with respect to ZnS as the incorporation of Fe causes the band gap narrowing and Fe 3d levels come to contribute to electronic band states in impurity levels [42, 45]. It is due to incorporation of Fe atoms and hence forming heterojunction between ZnS and FeS, or hybridization of d-orbitals or Fe substitution with Zn ions [45]. The reduction of the band gap helps it absorb a wider spectrum of visible light and also enhance charge separation, which would

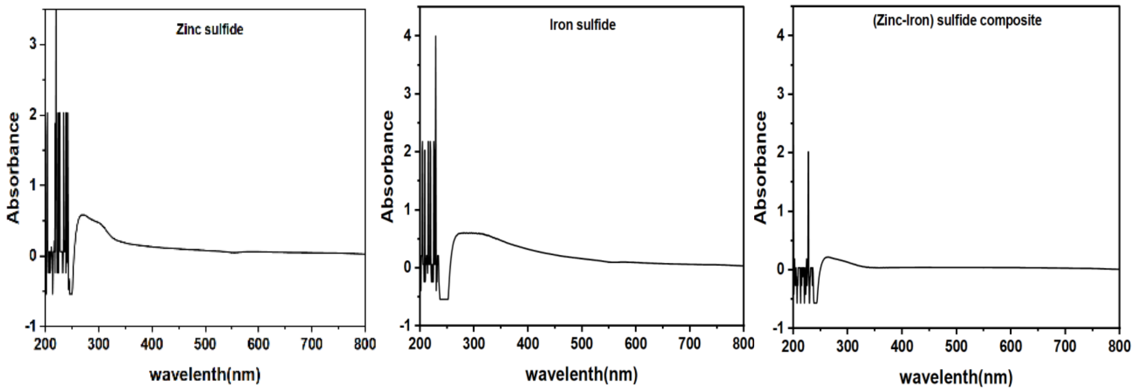

Fig. 6. Electronic spectra of zinc sulfide, iron sulfide and (zinc-iron) sulfide composite synthesized by precipitation technique.

Table 2. AFM data of zinc sulfide, iron sulfide and (zinc-iron) sulfide composite synthesis by sodium sulfide as precipitating agent.

Sample	Ra (nm)	Rq (nm)	Rt (nm)
ZnS	1.0	1.3	12
FeS	8.8	10.9	77
Zn–Fe–S	7.5	9.3	56

improve the performance as a photocatalyst. The precipitating agent sodium sulfide led to quick nucleation but has the drawbacks of high concentration of sulfur vacancies, lattice strain leading to localized electronic states, thus to band gap narrowing [46].

Fig. 7 compares theTG-DTA thermograms of zinc sulfide, iron sulfide and (zinc-iron) sulfide

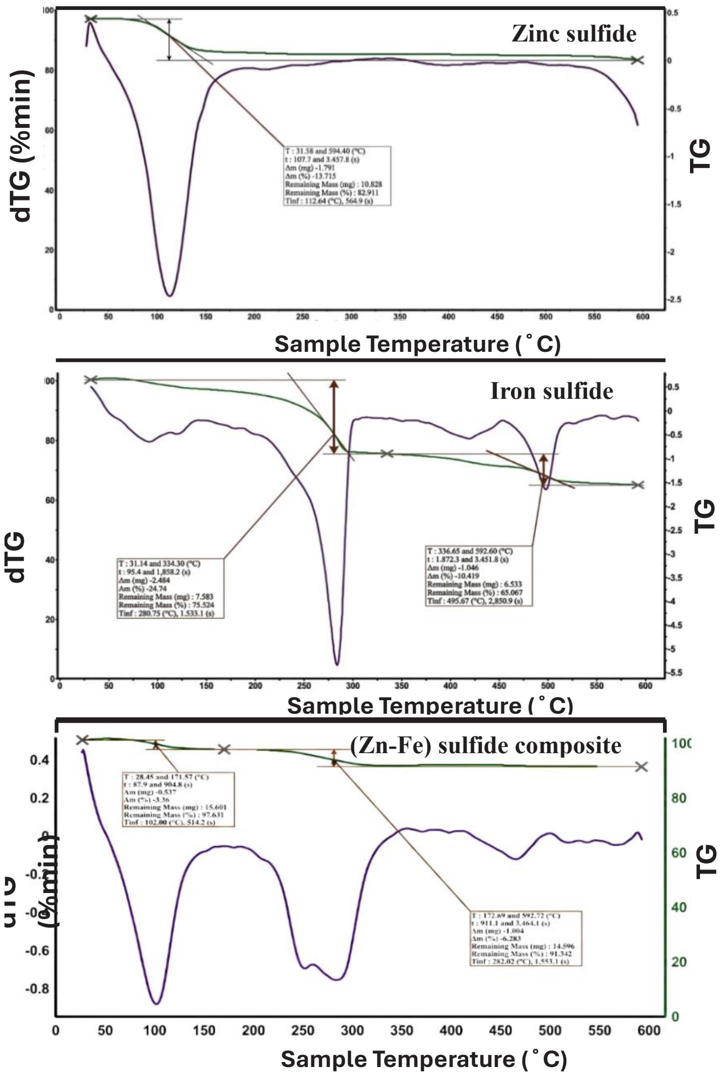

Fig. 7. TG-DTA thermograms of zinc sulfide, iron sulfide and (zinc-iron) sulfide composite synthesized by precipitation technique.

Table 3. Thermogravimetric data of zinc sulfide, iron sulfide and (zinc-iron) sulfide composite synthesis by sodium sulfide as precipitating agent.

Nanomaterials	(ΔE_a) (J/mol)	(ΔH) (J/mol)	(ΔS) ($J^{-1}k^{-1}mol^{-1}$)	(ΔG) (J/mol)
Zinc sulfide	61682.52	60746.03	210.102	37080.14
Iron sulfide	77425.05	75090.89	202.5091	18236.47
(Zinc-Iron) sulfide composite	49790.23	7614.574	202.4716	-49486.5

composite. Sodium sulfide is a source of S2 ions directly; so the formation of metal sulfides was very fast. The TG-DTG profiles were mainly correlated to the lost adsorbed water, subtle lattice restructure and stability as previously reported in the sulfides synthesized by inorganic sulfur sources [47,48]. TheZnS sample hasa total mass loss of about13.7% in range of 30-160 °C, which attributed to adsorbed water and solvent. A DTG peak located at 110-120 °C means mass loss from surface adsorbed specie (low bond strength). From 160 °C to 600 °C the mass shows an extremely stable plateau which represents the solid nature of the strongly bound Zn-S linkage and high stability which is characteristic of well-crystallized zinc sulfide nano particles [49]. The FeS also reveals a significant mass loss (about24.7%) in two steps (30-200 °C for moisture lose, 200-320 °C for structural rearrangement and loosely bound S lose). A higher mass loss and a main peak around 280-300 °C may mean more defects or other metastable phases exist in the structure. After 350 °C the FeS became quite stable as reported previously [50]. The least mass loss (~3.36%) for the (Zn-Fe)S composite shows the greatest thermal stability. A slightly lower mass loss below 100 °C corresponds to the loss of moisture, the second smaller peak between 170-300 °C relates to some slight lattice rearrange; above 300 °C it also remains very stable. It may result from the enhancement of stability due to

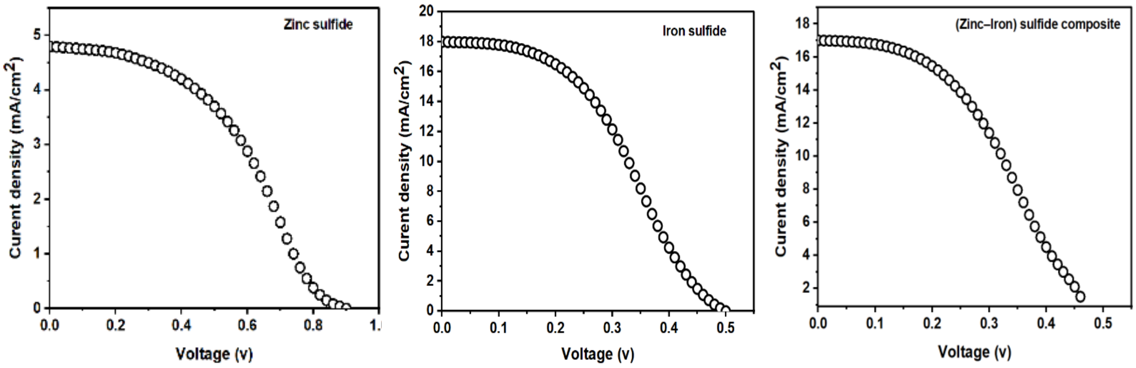

Fig. 8. J-V curves of zinc sulfide, iron sulfide and (zinc-iron) sulfide composite solar cells.

Table 4. Hall effect data of zinc sulfide, iron sulfide and (zinc-iron) sulfide composite synthesis by sodium sulfide as precipitating agent.

Sample	Conductivy (Old)	Bluk concetration (Old)	Mobility (Old)	(Hall Coefficient)
Zinc sulfide	0.28E-06	-2.51E+13	1.43E+01	-2.49E+05
Iron sulfide	6.36E-06	-9.87E+15	2.48E+02	-6.33E+02
Composite	7.33E-5	-4.55E+17	9.94E+02	-1.37E+01

Table 5. J-V curves of zinc sulfide, iron sulfide and (zinc-iron) sulfide composite solar cells.

Parameter	Zinc sulfide	Iron sulfide	(zinc-iron) sulfide composite
Jsc (mA/cm²)	5.5	19	18
Voc (V)	0.82	0.52	0.50
Jmax (mA/cm²)	3.0	12	11
Vmax (V)	0.60	0.40	0.38
FF	0.40	0.49	0.46
PCE / Efficiency (%)	1.8%	4.8%	4.2%

interaction of ZnS and FeS phases [51].

TGA data reveal the kinetic and thermodynamic behavior of zinc sulfide, iron sulfide, and their composite as demonstrated in Table 3. Iron sulfide shows the highest thermal stability with ΔEa of 77,425 J/mol, followed by zinc sulfide (61,682 J/mol), while the composite has the lowest (49,790 J/mol) due to synergistic interactions, defects, and better heat transfer that ease decomposition [52]. Enthalpy follows suit: iron sulfide and zinc sulfide need more heat, but the composite's low ΔH (7,614 J/mol) reflects structural disorder and lattice strain [53].

All samples have positive S, which represents an increase in the degree of disorder due to phase transition or gas evolution, with ZnS slightly higher than the others. Positive G means non-spontaneous reaction (both ZnS and FeS are positive), the negative G value in the composite (49,486J/mol) confirms the decomposition reaction (Fig. 5) is spontaneous [54]. It indicates that the composite would consume less energy, be more reactive and easier to be used for catalysis and energy applications [55].

The carrier types of the samples fabricated in the presence of NaS are n-type, the negative Hall coefficient was tested for the three samples and recorded in Table 4. It shows a sulfur-rich growth condition is employed, creating donor-type defects, for example sulfur interstitials and metal vacancies, so that the electrons are the dominant carriers [56,57].

The carrier concentrations and the relatively low mobility of the individual sulfide shows that the carrier scattering exists strongly at the grain boundaries and defect sites. Compared with single phase ZnS and FeS, the composite material exhibits an enhancement of conductivity and carrier mobility, which is mainly due to better carrier percolation and lower interfacial resistance of heterostructure network. There are many literatures reported the transport properties of sulfide composite materials prepared by rapid precipitation similar improvement [58,59].

The solar cell applications of the synthesized nanomaterials were tested as shown in Fig, 8. The J–V characteristics reveal clear differences in the photovoltaic performance of zinc sulfide, iron sulfide, and the (Zn–Fe) sulfide composite. Iron sulfide shows the highest efficiency (4.8%), followed by the composite (4.2%), while ZnS has the lowest efficiency (1.8%) as explained in Table 5. This trend is mainly due to variations in short-circuit current density (Jsc) and fill factor (FF).

The iron sulfide and the composite demonstrate high values for Jsc (19 and 18mA/cm2) which are expected values for narrow-bandgap materials with high absorption and charge generation [60, 61] whereas zinc sulfide demonstrates very low Jsc values (5.5mA/cm2) and low absorption. Zinc sulfide had the highest Voc (0.82V) which is attributed to the wide bandgap and low recombination within the material [62]. Fill factor was highest for iron sulfide (0.49) meaning less internal losses and lowest for zinc sulfide (0.40) as the material has higher resistive losses. Based on Jsc, Voc and FF values calculated and graphed efficiency is highest for iron sulfide due to the high current and the good FF value, Iron sulfide is the most efficient absorber material, composite has average absorption material qualities whereas zinc sulfide is more of an effective window or buffer layer rather than an absorption layer [63, 64].

CONCLUSION

We successfully prepared a Zn-Fe sulfide nanocomposite via simple chemical precipitation which showed good interaction between Zn and Fe ions, thus forming a mixed phase structure. A typical hybrid morphology which composed of spherical ZnS nanoparticles embedded into a porous FeS matrix was observed, which resulted in better surface area and interfacial contact. From optical properties, the band gap was narrowed down to 1.77 eV indicating enhanced visible light absorption, and electrical measurements reveal the n-type conductivity and charge transport were enhanced. Enhanced thermal stability also existed in composite as comparing to individual sulfides. Photovoltaic results indicated that the power conversion efficiency reached 4.2% which could be attributed to the enhanced separation efficiency and suppressed recombination. TheZn-Fe sulfide nanocomposite could be an ideal candidate as a cheap and high-efficiency material for photovoltaic application.

CONFLICT OF INTEREST

The authors declare that there is no conflict of interests regarding the publication of this manuscript.

REFERENCES

1. Isac L, Enesca A. Recent Developments in ZnS-Based

Nanostructures Photocatalysts for Wastewater Treatment. Int J Mol Sci. 2022;23(24):15668.

2. Pourjafari D, Saeednia S, Iranmanesh P, Hatefi Ardakani M. Preparation and Photocatalyst Properties of Zinc Sulfide Using a Distinct Sulfur Source: 1-Benzylidenethiourea. J Cluster Sci. 2019;30(3):571-580.
3. Saleem S, Khalid S, Malik MA, Nazir A. Review and Outlook of Zinc Sulfide Nanostructures for Supercapacitors. Energy AND Fuels. 2024;38(11):9153-9185.
4. Ali D, ElKatori E, Nagiub A. Synthesis, characterization, and heavy metal removal efficiency of zinc sulfide nanoparticles (ZSN's). Egyptian Journal of Chemistry. 2023;0(0):0-0.
5. Georgobiani AN, Gruzintsev AN, Volkov VT, Vorob'ev MO. Effect of annealing in oxygen radicals on luminescence and electrical conductivity of ZnO:N films. Semiconductors. 2002;36(3):265-269.
6. H2S/Curcumin Coreleasing Biomineralized Zinc Sulfide Nanostructures for Diabetic Wound Healing. American Chemical Society (ACS).
7. Ahmad RU, Javed N. Structure-Property Relationship in Zinc Sulphide Nanoparticles Synthesized by Hydrothermal and Co-precipitation Methods. Elsevier BV; 2026.
8. UK PubMed Central is hiring! : Front Matter; 2011.
9. Suroshe JS, Mlowe S, Garje SS, Revaprasadu N. Preparation of Iron Sulfide Nanomaterials from Iron(II) Thiosemicarbazone Complexes and Their Application in Photodegradation of Methylene Blue. Journal of Inorganic and Organometallic Polymers and Materials. 2018;28(3):603-611.
10. Structure-property relationships in PM iron-aluminium-silicon alloys. Metal Powder Report. 1998;53(10):38.
11. Kalantari S, Shokuhfar A. Diverse Utility of Cu Doped Zinc Sulfide/Iron Oxide Nanocomposites: Reusability, Adsorptive Properties, and Photocatalytic Efficacy in the Wastewater Purification. Research Square Platform LLC; 2023.
12. Constructing Heteroatom-Doped Transition-Metal Sulfide Heterostructures for Hydrogen Evolution Reaction. American Chemical Society (ACS).
13. Xia Y, Yu J. Metal Sulfide Semiconductor Photocatalysts. Semiconductor Solar Photocatalysts: Wiley; 2021. p. 269-298.
14. Salaheldin H, Aboelnga A, Elsayed A. Mycosynthesis of zinc sulfide/zinc oxide nanocomposite using Fusarium oxysporum for catalytic degradation of methylene blue dye, antimicrobial, and anticancer activities. Sci Rep. 2024;14(1).
15. Julnes G. Evaluation (2nd Edition), by Carol Hirshon Weiss, Upper Saddle River, NJ: Prentice Hall, 1998, 372 pp. The American Journal of Evaluation. 2001;22(2):265-268.
16. Post B. X-ray diffraction procedures for polycrystalline and amorphous materials. Harold P. Klug and Leroy E. Alexander, John Wiley and Sons, New York, 1974, pp. 960. $37.50. X-Ray Spectrom. 1975;4(4).
17. Suryanarayana C, Norton MG. Practical Aspects of X-Ray Diffraction. X-Ray Diffraction: Springer US; 1998. p. 63-94.
18. (Relativistic heavy ion research). Office of Scientific and Technical Information (OSTI); 1990 1990/01/01.
19. Pearson's crystal data: crystal structure database for inorganic compounds. Choice Reviews Online. 2008;45(07):45-3800-3845-3800.
20. Frasier KM, Rahni S, Ahmad U, B L, Dds G, Javaid S. A case report of spontaneous superficial temporal artery hemorrhage following COVID-19 infection. Open Journal of Clinical and Medical Case Reports. 2024;10(1).
21. Hargittai I. Christopher Hammond: The basics of crystallography and diffraction. Third edition. Struct Chem. 2009;20(4):751-751.
22. Cao G, Wang Y. Nanostructures and Nanomaterials: WORLD SCIENTIFIC; 2011 2011/01.
23. Sagnella DE, Foster E. Genie: new software for rapid submission of powder diffraction data to the ICDD powder diffraction file™. Powder Diffr. 2014;29(S2):S31-S34.
24. Kulkarni SK. Nanotechnology: Principles and Practices. Springer International Publishing; 2015.
25. Murray CB, Norris DJ, Bawendi MG. Synthesis and characterization of nearly monodisperse CdE (E = sulfur, selenium, tellurium) semiconductor nanocrystallites. Journal of the American Chemical Society. 1993;115(19):8706-8715.
26. Alivisatos AP. Semiconductor Clusters, Nanocrystals, and Quantum Dots. Science. 1996;271(5251):933-937.
27. Lin C-R, Lu S-Z, Lyubutin IS, Korzhetskiy YV, Wang S-C, Suzdalev IP. Synthesis and magnetic properties of iron sulfide nanosheets with a NiAs-like structure. J Appl Phys. 2010;107(9).
28. Wang X, Wei Q, Li H, Sun J, Li H, He Y, et al. Iron-chalcogenide-based electrode materials for electrochemical energy storage. Journal of Materials Chemistry A. 2022;10(14):7517-7556.
29. Yu XY, Lou XW. Mixed Metal Sulfides for Electrochemical Energy Storage and Conversion. Advanced Energy Materials. 2017;8(3).
30. Shi J. On the Synergetic Catalytic Effect in Heterogeneous Nanocomposite Catalysts. Chem Rev. 2012;113(3):2139-2181.
31. Burdett JK, Mitchell JF. Nonstoichiometry in early transition metal compounds with the rocksalt structure. Prog Solid State Chem. 1995;23(2):131-170.
32. Cantarero A. Review on Raman scattering in semiconductor nanowires: I. theory. Journal of Nanophotonics. 2013;7(1):071598.
33. CRC Handbook of Chemistry and Physics. CRC Press; 2014.
34. Gao R, Li Y, Zhang Y, Fu L, Li L. Defect-Mediated Energy Transfer Mechanism by Modulating Lattice Occupancy of Alkali Ions for the Optimization of Upconversion Luminescence. Nanomaterials. 2024;14(23):1969.
35. Behnia B, Aali Anvari A, Safardoust-Hojaghan H, Salavati-Niasari M. Positive effects of novel nano-zirconia on flexural and compressive strength of Portland cement paste. Polyhedron. 2020;177:114317.
36. Rao CNR, Müller A, Cheetham AK. Nanomaterials – An Introduction. The Chemistry of Nanomaterials: Wiley; 2004. p. 1-11.
37. Cian F. Clinical atlas of small animal cytology and hematology (2nd ed.) by AGBurton (Ed.), Hoboken, NJ, USA: Wiley-Blackwell. 2024. ISBN: 978-1119985624. $114. Vet Clin Pathol. 2024;53(4):458-459.
38. Williams DB, Carter CB. Scattering and Diffraction. Transmission Electron Microscopy: Springer US; 2009. p. 23-38.
39. Kauffman GB. Kenneth J. Klabunde and Ryan M. Richards (Eds): Nanoscale materials in chemistry, 2nd edn. Foundations of Chemistry. 2011;14(2):183-184.
40. Ferrari M. Introduction to Nanotechnology. Charles P. Poole, Jr., and Frank J. Owens. Hoboken, NJ: John Wiley and Sons, 2003, 400 pp., $79.95, hardcover. ISBN 0-471-07935-9. Clin Chem. 2004;50(5):981-981.
41. Cooke T. Wood Engineering and Construction Handbook.

3rd ed.991Keith Faherty, Thomas Williamson. Wood Engineering and Construction Handbook. 3rd ed. New York, NY: McGraw-Hill Handbooks 1999. pp. 889, ISBN: 0-07-022070-0 £71.99. Structural Survey. 1999;17(3):179-180.

42. Walker CT. Solid State Physics over 13 Years: Introduction to Solid State Physics . Charles Kittel. Wiley, New York, ed. 3, 1966. 662 pp., illus. $12.50. Science. 1967;155(3765):991-991.
43. Lee JH, Rizvi A, Lin FY, Min JK, Hartaigh Bó, Han D. Fractional Flow Reserve Measurement by Computed Tomography: An Alternative to the Stress Test. Interventional Cardiology Review. 2016;11(2):105.
44. Partee M. An Introduction to Christian Ethics by Robert H. Crook (3rd ed. Upper Saddle River, NJ: Prentice-Hall, 1999. 290 pp., pb. ISBN 0-13095131-5). Evangelical Quarterly. 2002;74(1):82-85.
45. Mohammad-Salehi H, Hamadanian M, Safardoust-Hojaghan H. Visible-Light Induced Photodegradation of Methyl Orange via Palladium Nanoparticles Anchored to Chrome and Nitrogen Doped TiO_2 Nanoparticles. Journal of Inorganic and Organometallic Polymers and Materials. 2019;29(5):1457-1465.
46. Behnia B, Safardoust-Hojaghan H, Amiri O, Salavati-Niasari M, Aali Anvari A. High-performance cement mortars-based composites with colloidal nano-silica: Synthesis, characterization and mechanical properties. Arabian Journal of Chemistry. 2021;14(9):103338.
47. Applications of Nanomaterials. Nanostructures and Nanomaterials: Published by Imperial College Press and Distributed by World Scientific Publishing Co.; 2004. p. 391-418.
48. The Chemistry of Nanomaterials: Wiley; 2004.
49. Skoog DA, Holler FJ, Crouch SR. Molekülllumineszenzspektroskopie. Instrumentelle Analytik: Springer Berlin Heidelberg; 2013. p. 397-425.
50. Habashi F. The Future of Copper Metallurgy. Miner Process Extr Metall Rev. 1995;15(1-4):5-12.
51. Poole CF. Chromatography: Concepts and Contrasts. Chromatographia. 2010;72(3-4):369-369.
52. Khawam A, Flanagan DR. Solid-State Kinetic Models: Basics and Mathematical Fundamentals. The Journal of Physical Chemistry B. 2006;110(35):17315-17328.
53. Brown ME, Gallagher PK. Introduction to Recent Advances, Techniques and Applications of Thermal Analysis and Calorimetry. Handbook of Thermal Analysis and Calorimetry: Elsevier; 2008. p. 1-12.
54. Logvinenko VA. Some macrokinetic structural aspects of heterogeneous thermal dissociation reactions. Thermochim Acta. 1987;110:159-163.
55. Aylett BJ. Transition Metal Oxides: Structure, Properties and Synthesis of Ceramic Oxides. C.N.R. Rao and B. Raveau. 2nd edn. Wiley–VCH, New York and Weinheim, 1998. xi + 373 pages. £80. ISBN 0-471-18971-5. Appl Organomet Chem. 1999;13(6):476-477.
56. Bennett G. Standard handbook of hazardous waste treatment and disposal H.M.Freeman (Ed.), McGraw-Hill, New York, NY, 1989, ISBN 0-07022042-5, 1120 pp., $89.50. J Hazard Mater. 1991;26(3):373-374.
57. Altomare A. Solid-state properties of pharmaceutical materials. Crystallography Reviews. 2019;26(2):115-116.
58. Brock SL. Nanostructures and Nanomaterials: Synthesis, Properties and Applications By Guozhang Cao (University of Washington). Imperial College Press (distributed by World Scientific): London. 2004. xiv + 434 pp. $78.00. ISBN 1-86094-415-9. Journal of the American Chemical Society. 2004;126(44):14679-14679.
59. Nanoscale Materials in Chemistry: Wiley; 2009.
60. Norcia VD. Corporations and MoralityThomas Donaldson Englewood Cliffs, NJ: Prentice-Hall, 1982. Pp. ix, 214. $12.95, cloth; $8.95, paper - Business EthicsNorman Bowie Prentice-Hall Series in Occupational Ethics Englewood Cliffs, NJ: Prentice-Hall, 1982. Pp. xiii, 159. $7.95, paper. Dialogue. 1983;22(2):364-366.
61. Handbook of Photovoltaic Science and Engineering: Wiley; 2010.
62. Transparent Conductive Zinc Oxide. Springer Series in Materials Science: Springer Berlin Heidelberg; 2008.
63. Sze SM, Ng KK. Physics of Semiconductor Devices: Wiley; 2006 2006/04/10.
64. Nelson, Prof. Jenny, Professor of Physics, Blackett Laboratory, Imperial College London, since 2006. Who's Who: Oxford University Press; 2016.